Activation volume and the role of solute atoms in Al-Mg-Si alloy processed by equal channel angular extrusion

Amel Soula, Jean Philippe Couzinié, Hanen Heni, Julie Bourgon, Yannick Champion, Nabil Njah

Activation volume and the role of solute atoms in Al-Mg-Si alloy processed by equal channel angular extrusion

Amel Soula[a], Jean Philippe Couzinié[b], Hanen Heni[a], Julie Bourgon[b], Yannick Champion[b,1], Nabil Njah[a,*]

[a] *GEOMAT,Laboratoire Georessources Environnement Materiaux et Changements Globaux, Faculté des Sciences de Sfax, Université de Sfax, PB 1171, 3000 Sfax, Tunisia*

[b] *Univ Paris Est Creteil, CNRS, ICMPE, UMR 7182, 2 rue Henri Dunant, 94320 Thiais, France*

Keywords:
Al-Mg-Si
alloys ECAE
ASTAR
imaging SRS
Activation volume

a b s t r a c t

Grain refinement to the sub-micron scale was found to enhance both strength and plasticity. In this size range, the micro-mechanisms of deformation are not yet sufficiently specified. In the present work, strain rate sensitivity was investigated in an Al-Mg-Si alloy processed by equal-channel angular extrusion. The microstructure was controlled by conventional transmission electron microscopy and orientation imaging- ASTAR. In the as-quenched state, deformation produces grains below 100 nm in size. The activation volume V was reduced to $70b^3$. Based on published theoretical models, we have shown that in such alloy, pure grain boundary sliding cannot be revealed in the low-stress range, due to the intervention of solute atoms. Beyond, the stress-dependence of V consists with an inverse Cottrell-Stokes behavior. This trend was confirmed by TEM which revealed dislocation activity and grain boundary emission. Ageing at 150 °C in- creases the contribution of GBS whereas the residual activation volume continues to be leveled.

1. Introduction

The development of alloys with advanced properties has taken a great importance for the last decades. In particular, alloys for automotive are of a particular interest due to the complex shaping required for sheets. In mechanical forming like deep drawing, the problem of necking i.e. local thinning constitutes a limitation for achieving complex shapes since the latter require a high plasticity before failure [1]. The stress at failure is generally predicted by the Considère's criterion $(1/\sigma)\, d\sigma/d\varepsilon < 1$ where σ and ε are the true stress and true strain respectively [2–5]. Nevertheless, it has been shown that the instability is delayed and ductility is increased if the alloy exhibits a strain rate sensitivity (SRS) and the criterion becomes $(1/\sigma)\, d\sigma/d\varepsilon + m_s < 1$ [6] where $m_s = \left(\frac{d\ln\sigma}{d\ln\dot{\varepsilon}}\right)_{\varepsilon,T}$ is the strain rate sensitivity parameter. On the other hand, it has been shown that low values of m can be compensated by low strain hardening [7]. Strain rate jump experiments are frequently used to study the SRS which is related to the nano-scaled deformation mechanisms. SRS arises from the rate equation for plasticity [1]: In thermal activation analysis, the shear strain rate is given by:

$$\dot{\gamma} = \dot{\gamma_o} \exp\left(\frac{-(\Delta G^{o}* - \tau* v*)}{kT}\right) \quad (1)$$

$v* = \frac{\partial \Delta G}{\partial \tau*}$ is the activation volume of the activated process; obviously, it means the unit volume of the crystal directly affected by the dislocation movements [8] or the region swept by a dislocation [9,10]. $\tau* = \tau - \tau_a$ is the shear stress responsible of dislocation motion which is strain rate dependent, τ is the applied or experimental shear stress, τ_a the athermal component due to the intrinsic resistance of the lattice to flow, k the Boltzmann constant and T the working temperature. A macroscopic (apparent) activation volume V can be obtained experimentally from the strain rate dependence of the flow stress; this needs to link the experimental data σ and ε to τ and γ respectively. Thus, writing $\tau = \sigma / M$ where M is the Taylor factor and $\sigma* = \sigma - \sigma_a$, Eq. (1) can be identified to:

$$\dot{\varepsilon} = \dot{\varepsilon_o} \exp\left(\frac{\left(\Delta G^{o}* - \left(\frac{\sigma* v*}{M}\right)\right)}{kT}\right) \quad (2)$$

Dislocation propagation is the common deformation controlling mechanism in conventional alloys. The dislocation velocity depends

on their interaction with obstacles mainly forest dislocations, solute atoms, precipitates, and grain boundaries. However, when grain size is reduced to few nanometers, grain boundary sliding (GBS) becomes important. Transition from dislocation to GBS for very fine grain sizes depends on the different contributions in the mobile dislocation interactions, i.e. the microstructure. Several attempts have been made to formulate the various contributions. A model has been developed by Duhamel et al. [11] and modified by Champion [12]. They have shown that the total shear strain rate can be defined by:

$$\dot{\gamma} = \frac{\rho_m bd}{t_e} + \frac{\delta}{d.\, t_{gb}}. \quad (3)$$

ρ_m is the mobile dislocation density, b the magnitude of the Burgers vector of dislocations, d the grain size (GS), δ the width of the grain boundaries (GBs), t_e the emission time of dislocations from sources near GBs, t_{gb} the time for an elementary GB displacement δ. t_e and t_{gb} are kinetic parameters which reflect thermally activated processes mainly diffusion within GBs and nucleation of dislocations in the vicinity of GBs [11]. The first term in the right hand side of Eq. (3) is the rate of dislocation straining and the second term is the rate of GB one. The critical grain size below which GBS becomes dominant is obtained by equalizing the two terms in the right hand side of Eq. (3): $d_c = \sqrt{\frac{\delta t_e}{\rho_m b t_{gb}}}$. The competition between GBS and DS and their relative importance depend on GS and lead to different dependencies of V on the shear stress [11]: At very low grain size where GBS is dominant V is a constant ≈Vc (regime I). However, a constant value of V can also be obtained when the thermally activated motion of dislocations is related to their interaction with solute atoms rather than to the intersection of dislocations [13]; this feature will be discussed in detail in Section 4. When the grain size increases, the contribution of the mobile dislocations becomes important, V∝τ which was identified as the inverse Cottrell-Stokes behavior (ICS, regime II). For the conventional grain size, V∝1/τ, i.e. a Cottrell-Stokes behavior [14] (CS, regime III). Quantitatively, these mechanisms result in values of V differing by one to three orders of magnitude [15]: For the conventional GS (1 μm to 1 mm) where all types of deformation are operative (slip and twinning with possible dislocation pile-ups), V 100–1000b^3. In the GS range between 10 nm and 1 μm, deformation remains trans-granular with dislocation emission from GBs and without need of pile-ups; V 20b^3 for GS of 10–100 nm and 100–300b^3 for GS of 6–40 μm [16]. For these two regimes, V decreases with decreasing grain size and increasing strain consistent with a CS behavior. For GS below 10 nm, a grain size softening was observed [16]; V 10b^3 and 1–1.2b^3 which were attributed to GBS and to atomic diffusion in GB or through the crystalline lattice respectively [17].

From the above considerations, grain refinement to few nanometers remains among the procedures of obtaining materials with advanced properties. To this end, several thermomechanical methods have been used to produce nanograined materials. Equal channel angular extrusion (ECAE) is the most used tool since it can be applied to metallic materials without a change in the specimen shape [18,19]. Many subsequent changes were introduced in the die shape or in the feeding procedure leading to derivative techniques like continuous equal channel angular pressing applied to strips [20]. However, the main inconvenient of ECAE is the achieved grain size which is limited to 100 nm. High pressure torsion [21] produces grains below 100 nm but the small specimen size prevents a possible industrial application. Recently, rotary swaging was used to refine grains in Mg alloys and can also be applied to alloys of a low cold workability [22,23]; thus grains of 80 nm in size were obtained in Mg–Gd–Y– Zr alloy [24]. It is worth recalling that in practice, controlling grain size in the nanometer range is difficult since the non-equilibrium state is the common character of the obtained microstructures [25]. On the other hand, alloying seems to preserve the sub-micron grain size through a limitation of diffusion-controlled growth [26,27].

The studies of the effects of severe plastic deformation SPD on the mechanical properties have been focused on the strength characteristics i.e. the yield stress and the ultimate tensile strength UTS in relation with structural applications [28–31]. The important results are still limited to a high flow stress but at the expense of ductility. After ECAE, few alloys exhibited superplasticity at low strain rates and high temperatures [32] and others at high strain rates and low temperatures [28]. In pure metals the substantial reduction of grain size by ECAE leads to a transition from dislocation sliding to intergranular one in order to enhance plasticity [33,34]. In alloys, the micro-mechanisms of deformation after SPD become more difficult to explain due to the contribution of many factors like forest-dislocations, solute atoms and precipitates.

In the present work, the effects of ECAE on the microstructure and on the SRS of an Al-Mg-Si alloy of the 6000 family were investigated. In fact, these are precipitate-hardened alloys and candidate for automotive applications [35]. After appropriate ageing treatments, the microstructure is formed by an Al-matrix and Mg_2Si precipitates. Like other aluminum alloys, a precipitation sequence from a saturated solid solution (SSS) consists in SSS→GP→ β″ →β′→β where GP is the Guinier-Preston clusters, β″ and β′ are transient phases and β is the equilibrium Mg_2Si phase. In such alloys, ECAE employed for grain refinement was found to enhance the precipitation kinetics due to the high dislocation density and to the high volume fraction of grain boundaries introduced [36–40]. Furthermore, a modification of precipitation sequences is occasionally observed in comparable alloys like Cu-Al with an eventual suppression of intermediate phases [41].

Compared to steels, aluminum alloys have a small SRS unless at room temperature [42] but their low density justifies the SRS investigation mainly if the achieved flow stress is close to that of low-carbon steel [1]. The development of advanced imaging techniques like EBSD in SEM and ASTAR-MEGASTAR in TEM provides precious tools for the microstructure characterization through different manners in exploring diffraction patterns. We have used ASTAR-MEGASTAR in addition to conventional TEM imaging to characterize the microstructure in term of grain and precipitate morphology. Transient strain rare jump tests in compression were used to investigate the SRS and the activation volume of deformation after ECAE. Aging effect after ECAE was also investigated to check the effects of precipitation on the SRS. The experimental results were interpreted referring to published theoretical models.

2. Experimental

The investigated material is an industrial Al-Mg-Si alloy of the 6xxx family. The chemical composition was determined by X-Ray fluorescence (XRF) (Table 1).

The alloy was annealed at 500 °C for 24 h and quenched in iced water to produce homogeneity. ECAE experiments were performed at room temperature on specimens 10 × 10 × 70 mm^3 in size in the as quenched state. The die is formed by two channels intersecting at an angle ϕ = 90°. The angle Ψ representing the outer arc of curvature is 90°. In these conditions, the total strain, ε_N, accumulated by N passages through the die is ε_N = 0.906 N [43]. Specimens were extruded up to four times via route B_C using a hydraulic press under a pressure of 200 MPa at a rate of 5 mm/min; they were coated with a lubricant containing MoS_2 before introduction in the channel. Samples

Table 1
Alloy composition.

	Mg	Si	Fe	Al
wt%)	1 – 1.2	0.5 – 0.6	0.2	Balance

for TEM were cut from the billets in the plane normal to ECAE direction. They were mechanically grounded to a thickness of 100 µm and punched. Many specimens were then aged at 150 °C for different times. The TEM foils were thinned by twin-jet technique in a solution of 33% nitric acid in methanol at − 30 °C. As the interest in reliable and efficient characterization of nanomaterials is growing, TEM was completed with orientation imaging - ASTAR package which is an automatic crystallographic orientation and indexing tool developed for TEM [44]. It provides much complementary information such as orientation relations between matrix and precipitates (epitaxy) and grain orientation distribution (texture). ASTAR imaging in defining grain morphology provides a more filtered microstructure as compared with conventional TEM imaging. For this purpose, the TEM is set in nano-beam mode and the incident electron beam is scanned over the area of interest at a high rate (typically 100 points per second). Virtual images (bright field or dark field) are obtained by "inserting" a virtual objective apearture on the transmitted or diffracted beam. The distribution of phases and grain orientation maps were determined with an Automatic Crystal Orientation Mapping (ACOM) system installed in a FEI Tecnai F20 TEM. An ASTAR system was used for ACOM diffraction data acquisition. The analyzed map step was 10 nm based on a square grid. The identification of phases and orientations are obtained through image matching between experimental diffraction patterns and calculated templates.

Strain rate sensitivity in mechanical tests was investigated to check the effects of ECAE and precipitation on the activation volume of deformation V* . For this purpose, compressive strain-rate jump tests were carried out at room temperature using a MTS 20/M machine. The strain rates investigated ranged between 10^{-5} and 10^{-3} s^{-1}. In fact, compared to straining specimens at different strain rates, jump test on a same specimen has the advantage that it leads to an activation volume independent of the theoretical model involved [45].

3. Results

3.1. As deformed state

Bright field image and SAD pattern of the alloy after ECAE for N = 4 are shown in Fig. 1. Diffraction pattern shows a significant refinement of the whole microstructure which was decreased to the sub-micron scale. Many grains are separated by well-defined boundaries as revealed by the fringe contrast (arrowed).

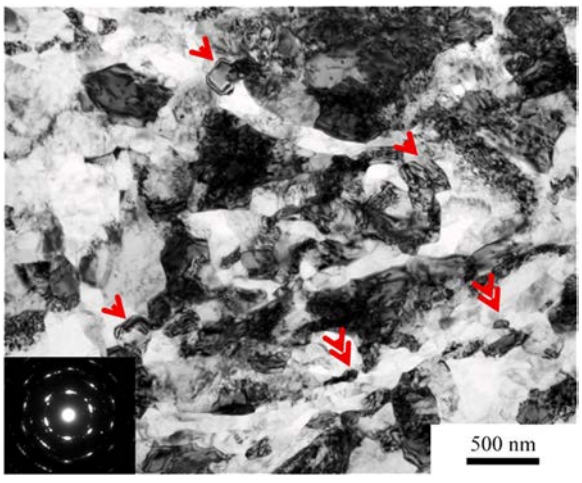

Fig. 1. Bright field TEM image and the corresponding SAD pattern after ECAE (N = 4). SAD shows a clear refinement of the microstructure. Many high angle boundary grains 100–200 nm in size are arrowed.

Furthermore, grains 100–200 nm in size are revealed (double arrows). Fig. 2 represents the microstructure of the alloy for N = 4 in two different areas as revealed by ASTAR imaging with respect to X and Y axes. Small equiaxe grains are observed in virtual bright field (VBF) and orientation images (arrowed in Fig. 2a and b) and which were not clearly revealed by conventional TEM. From the phase mapping of Fig. 2d, these correspond to pure silicon. Thus, as the present alloy is of high silicon content (high Si/Mg ratio), small eutectic areas containing pure silicon were deposited. Since silicon has a diamond cubic lattice, the color code applied to aluminum matrix reveals also silicon grains. The distribution of the latter shows that it coats in part the pre-existing grains boundaries. The same morphology of silicon crystals was revealed in EBSD imaging of a casting Al-7%Si alloy [46].

3.2. Aging effect

In such alloy, heating leads to the precipitation of hardening phases and in deformed specimens to a possible recovery of the microstructure in term of dislocation annihilation and rearrangement. Fig. 3 shows the morphology of grains after annealing of the ECAE processed alloy at a moderate temperature (N = 4 + 1 h at 150 °C). We note the formation of equilibrium grains 100–200 nm in size with well-defined grain boundaries. Furthermore, many remaining dislocations are still present and seem to be coated with precipitates. ASTAR images of specimens extruded for N = 2 and N = 4 after annealing are given in Fig. 4. VBF images show grains of ≈ 200 nm in size many of them are marked (Fig. 4); no clear difference is remarked between N = 2 and N = 4. According to the color code used (Fig. 2h), many grains seem to have the same orientation.

TEM micrographs of the deformed alloy after annealing for 1 h at 150 °C are shown in Fig. 5. As was revealed by ASTAR imaging, grain size remains in the sub-micron range. Needle-shaped precipitates are formed. According to previous investigations, they represent the β″ phase of monoclinic structure and which are present up to the aging peak [36,47,48]; WBDF images show that precipitation is located preferentially on dislocations and dislocation walls.

In order to determine the elementary mechanisms of deformation after ECAE, strain rate jump tests were performed. Fig. 6 shows the compression curves of the alloy after ECAE before and after aging at 150 °C. The alloy exhibits a flow stress of 300 MPa, 309 MPa and 317 MPa for N = 2, N = 3 and N = 4 respectively versus 80 MPa before ECAE (N = 0). In all the deformed specimens, the strain hardening after ECAE, i.e. the mean slope of the plastic part of the curve is small and does not exceed 25 MPa whereas it is close to 700 MPa before ECAP. Significant strain rate sensitivity is remarked for N > 2. Annealing behavior was investigated for N = 2 and N = 4. A decrease of the 0.2% flow stress is observed in the ECAE processed alloy whereas an increase is observed in the as quenched alloy (N = 0). All the deformed specimens exhibit a significant SRS.

4. Discussion

The rings observed on the diffraction pattern of Fig. 1 indicate a substantial refinement of the microstructure. Moreover, BF image reveals many grains with equilibrium high angle boundaries (arrowed); this microstructure is generally reached in the advanced stages of deformation and may indicate a saturation amount of strain. ASTAR images of Fig. 2 show elongated grains clearly revealed with respect to Y axis (Fig. 2f, g). With respect to X, a small ambiguity in orientation mapping is revealed; this is related to the fact that the present experiments have been performed without precession of the incident beam. Consequently, the orientation map generated results occasionally in inconsistent index over areas that must have uniform orientation. Furthermore, referring to the stereographic triangle (Fig. 2h), the orientation seems to not vary much over the same

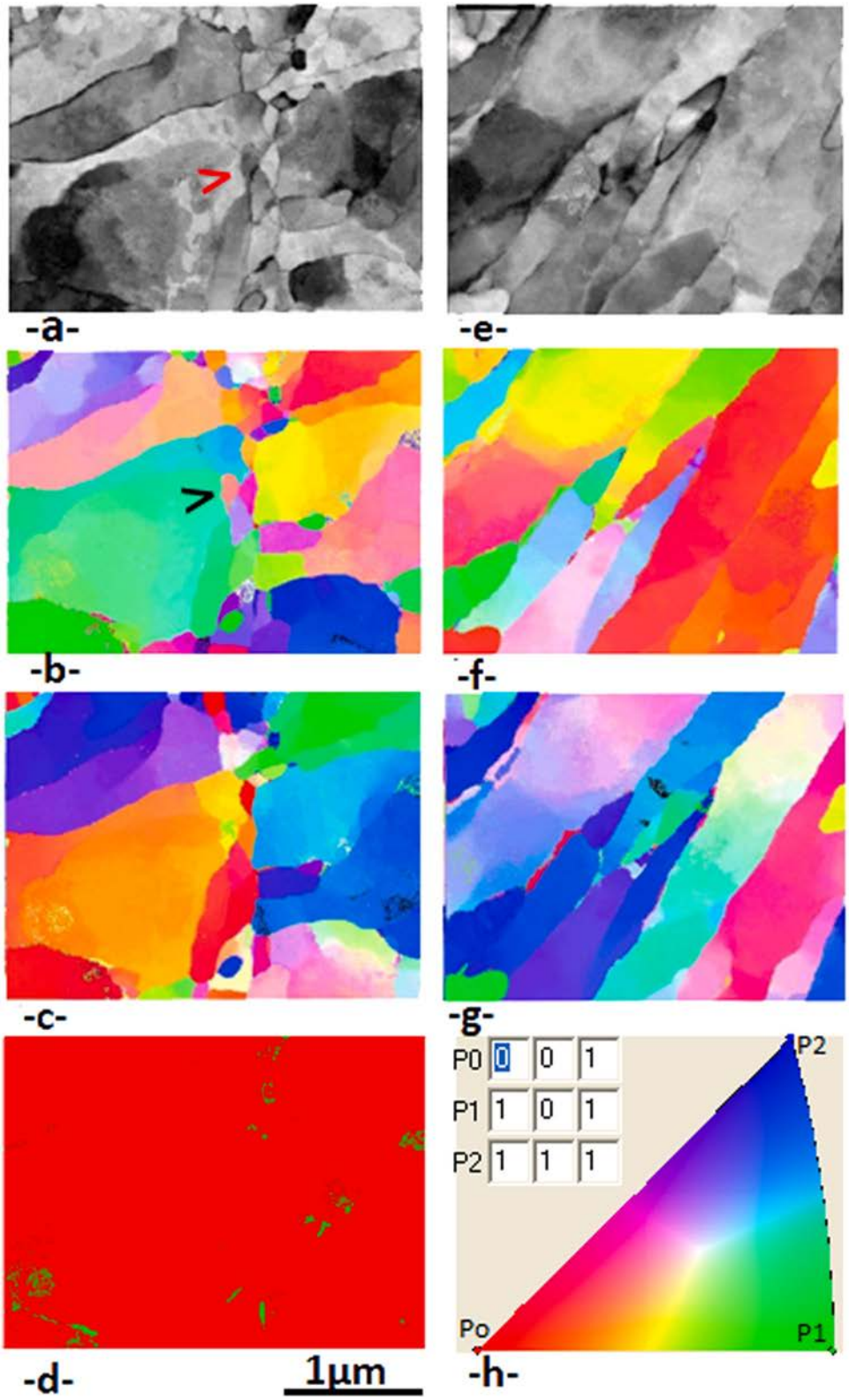

Fig. 2. N = 4, two zones (column 1 (a-c) and column 2 (d-f)): (a, e) VBF images, (b, f): crystal orientation maps with respect to X, (c, g) crystal orientation maps with respect to Y, (d) Silicon phase mapping, (h) color key for the cubic crystal orientation maps.

grain. It is clear that VBF images (Fig. 2a, b) are smoother than the conventional BF one (Fig. 1); this is because ASTAR images are not sensitive to strain.

The increase in the flow stress after ECAE is due to the increase in dislocation density. The increment of the flow stress for N = 4 is 231 MPa. Using the Orowan equation [49,50].

$$\Delta\sigma=\alpha MGb\rho^{1/2} \quad (4)$$

where $\Delta\sigma=\sigma_N-\sigma_{N=0}$, α is the obstacle strength associated with the forest dislocations, G is the shear modulus, b the dislocation Burgers

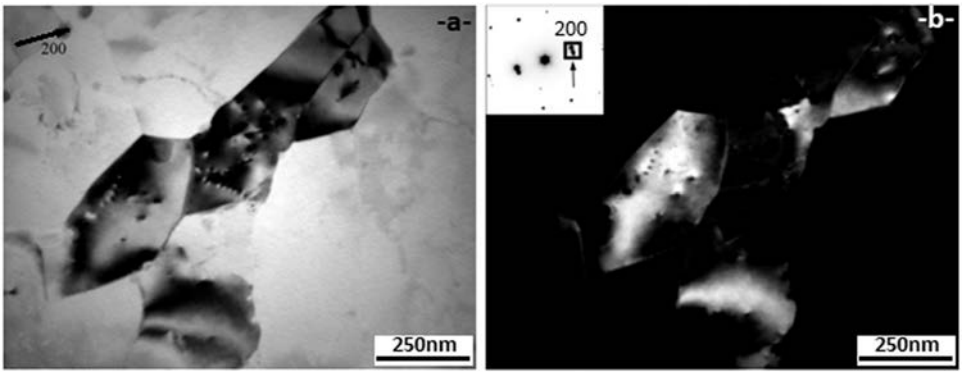

Fig. 3. BF and DF TEM images of the alloy for N = 4 and aging for one hour at 150 °C. Grains 200 nm in size with equilibrium grain boundaries are formed.

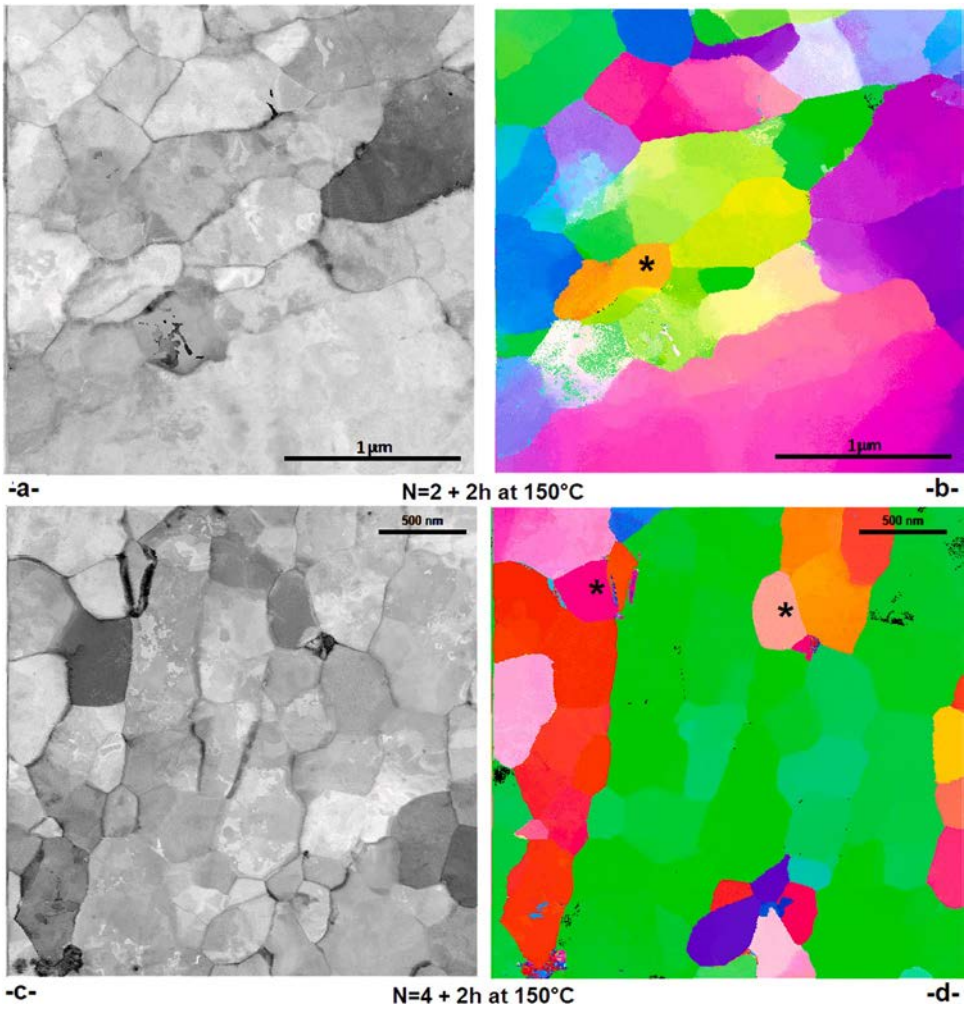

Fig. 4. Virtual bright field images and crystal orientation maps of the alloy after ECAE and aging: a, b: N = 2 + 150 °C/2 h; c, d: N = 4 + 150 °C/2 h.

vector, M is the Taylor factor. Taking $\alpha \approx 0.3$ [1], G= 25 GPa [1], b= 0.286 nm [32]; $M=\sqrt{3}$ in nanocrystalline materials [11,52], the corresponding dislocation density is $\rho = 4.10^{15}\,m^{-2}$. This value is quite higher than that generally obtained in equivalent alloys after ECAE ($\approx 10^{14}\,m^{-2}$ [46,52]); this results from an overestimation of the dislocation contribution in the flow stress. Thus, because of its higher radius (0.160 nm) as compared to aluminum (0.145 nm), Mg tends to segregate to dislocations and clusters can form inducing a further hardening (strain aging). On the other hand, even though TEM and XRD did not reveal any precipitation in quenched and deformed alloys, precipitation of fine β″ particles few nanometers in size was evidenced by HRTEM after ECAE at room temperature in 6013 aluminum alloy [53]; this results in an increase in the measured flow stress.

Magnifications of the plastic part of the curves of Fig. 6 are given in Figs. 7 and 8. A significant sensitivity to strain rate is observed since N = 2. Beside, a transient peak is remarked on the compression curves for all the changes in the strain rate. Because of this transient regime it is not trivial to calculate the SRS since it should differ by an order of magnitude when considering the transient stress (TS) at the

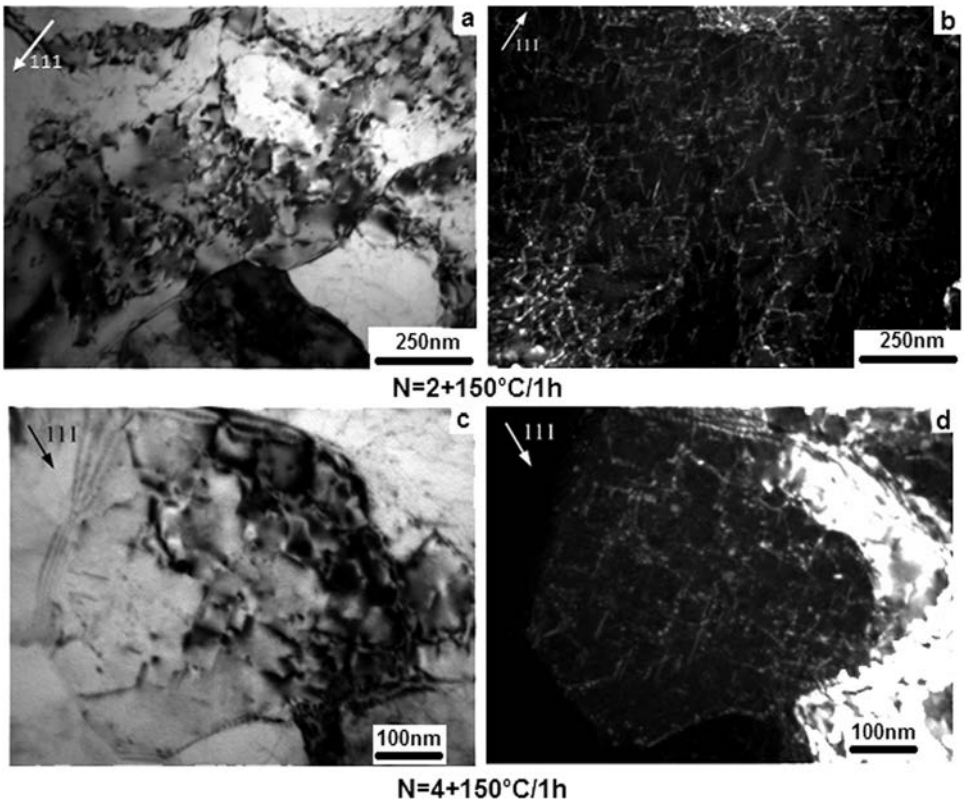

Fig. 5. Weak-beam bright field (WBBF) and weak-beam dark field (WBDF) images of the alloy after ECAE and aging: a, b: N = 2 + 150 °C/1 h; c, d: N = 4 + 150 °C/1 h.

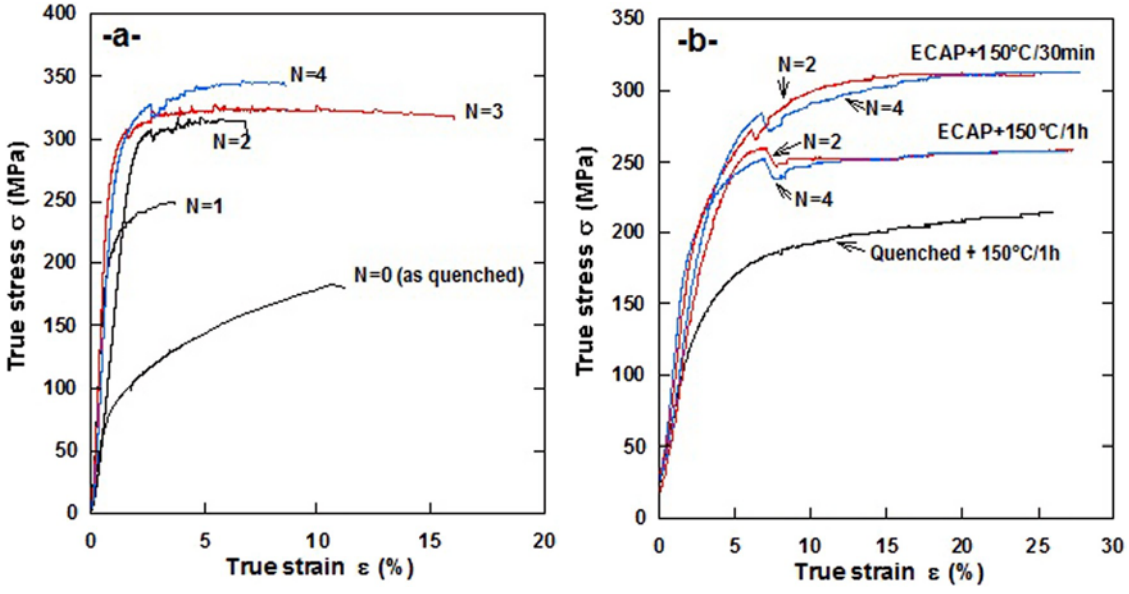

Fig. 6. Stress-strain curves in compression of the alloy processed by ECAE before ageing (a) and after aging at 150 °C (b).

peak or beyond, i.e. the steady state stress (SSS) [54]. In many investigations, TS was related to a non-ideal compensation of the specimen elastic strain accompanying the change of the flow stress due to the strain rate change by the testing system [55,56]. For this reason, to avoid complexity introduced by the system compliance up-jumps are generally preferred to down- jumps [51]. The presence of TS and SSS has been observed in several investigations and has been interpreted differently: McCkromick [57] has attributed the transient peak in continuous straining of Al-Mg-Si alloy to the formation of Lüder bands which traverse the gauge length. The author suggests that the main effects of the increase of the strain rate is the increase of the band velocity and hence in the dislocation velocity [57]. In nanocristalline BCC tantalum (Ta) deformed at 77 K, the transient peak was attributed to the low mobility of screw dislocations controlling the deformation at this temperature [58]. In ultrafine grained aluminum alloys, yield peak was interpreted by a pinning of mobile dislocations by solute atoms [59]. In fact, when reaching an obstacle, a dislocation has to wait for a given time t_w until the obstacle is overcame. The waiting time depends on the energy barrier which has to be overcome. After, the dislocation

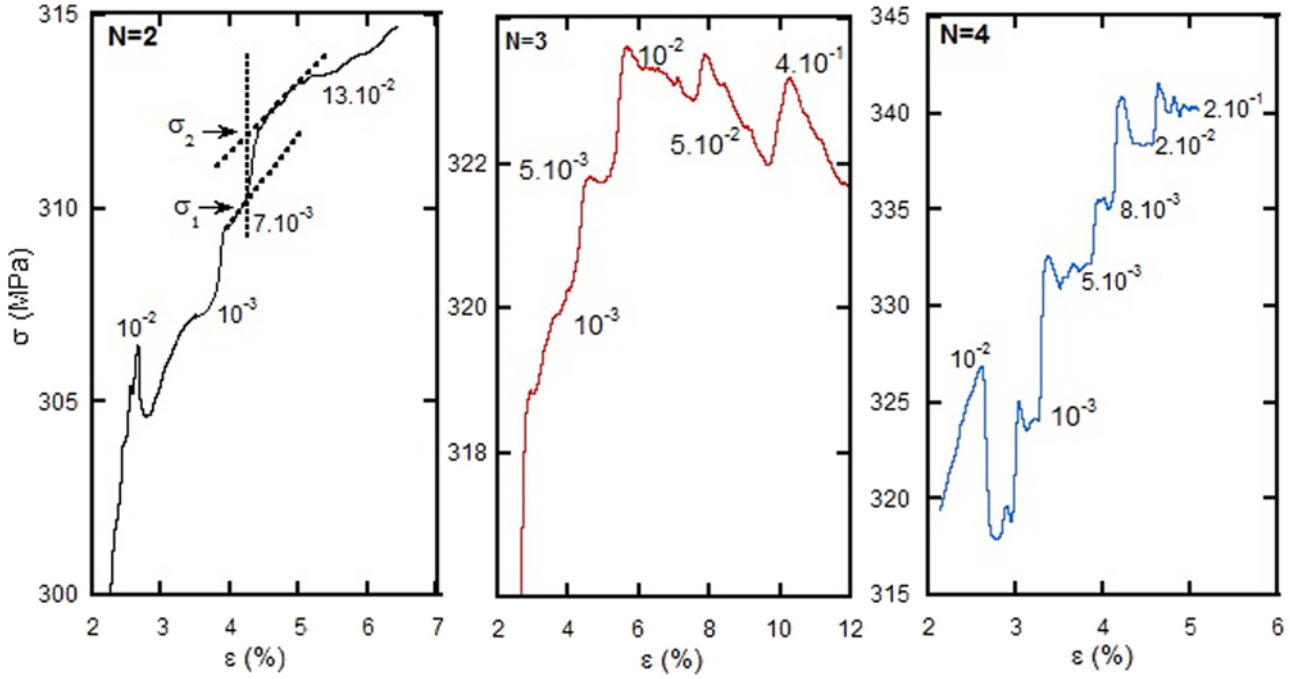

Fig. 7. Magnification of the plastic part of the curves of Fig. 6 for N = 2, N = 3 and N = 4 with the corresponding strain rates (s^{-1}). Example of the steady state stress determination is shown for N = 2.

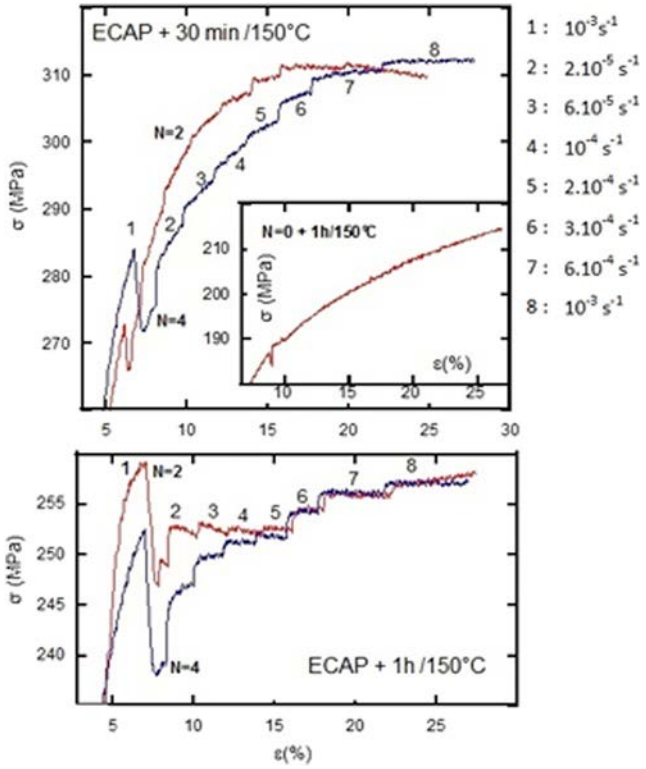

Fig. 8. Magnification of the plastic part of the curves of Fig. 6 for N = 2 and N = 4 after aging for 30 min and 1 h at 150 °C. The corresponding strain rates (s^{-1}) are indicated.

jumps with a high velocity until reaching another obstacle. During this period t_w, solute atoms segregate to dislocations and pin them; this is known as dynamic strain aging (DSA). Accordingly, the dislocation velocity is $v_d = L/t_w$ where L is the mean distance between obstacles [59]. Furthermore, by considering $v_d = f(\sigma)\exp-Q/RT$ [60] and the equation $\dot{\varepsilon} = \rho_m b v_d$, t_w depends on the SR as $t_w = \rho_m bL/\dot{\varepsilon}$ [61].

The time required for interstitial atoms to reach the blocked dislocation, i.e. aging time, ta is diffusion- dependent [57]; the model assumes that dislocation is locked when $t_w = t_a$ which occurs at a critical strain ε_c. In practice, the width of the transient peak should be a direct measure of t_w. Thus $t_w = \Delta\varepsilon/\dot{\varepsilon}$ where $\Delta\varepsilon = \varepsilon_{sss} - \varepsilon_{TS}$ (in the narrow interval $\Delta\varepsilon$ considered, ρ_m is considered to be constant). For N = 4, the stress reached its steady state (SS) value after 0.24% of strain. Accordingly, t_w was calculated to be 47 s and 11 s at $\dot{\varepsilon} = 5.10^{-5}$ s^{-1} and 2.10^{-4} s^{-1} respectively. These values are of the same order as the value 100 s deduced from the results of van Petegem et al. [25] in nanocristalline Ni-Fe alloy in which the stress reaches its SS value after 0.5% of strain. Nonetheless, their larger peaks should be related to a higher energy of solute-dislocation bond and to a lower density of mobile dislocations. It is worth noting that in all cases, TP are clearer at low strain rates; this was explained by the temperature compensation by stain rate from the Zener law [61].

Due to the above considerations, in the present work, SRS was calculated rather from the SSS before and after SR jumps. SSS beyond a peak was determined by extrapolating the curve to the strain ε_1 relative to σ_1 as shown in Fig. 7.

The values of m were used to calculate the apparent activation volume V from the experimental dependence of σ on $\dot{\varepsilon}$ $V = MkT/m$ where $m = \left(\frac{\Delta\sigma}{\Delta \ln\dot{\varepsilon}}\right)$. Fig. 9 represents the evolution of V as a function of σ. We note that since N = 2, V exhibits a constant value V* below a critical flow stress σ_c followed by a domain where $V \propto \sigma$. These different dependencies of V against the applied stress arise from different deformation mechanisms in the present alloy.

4.1. The constant values of the apparent activation volume V*

The obtained values of V* are close to $160b^3$, $100b^3$ and $75b^3$ for N = 2, N = 3 and N = 4 respectively. These high values as compared with 10–$20b^3$ reported for GBS [11,17,18], and their dependence on N show that the constant value cannot be attributed to a pure GBS. Furthermore, it has been reported [11,61–63] that GBS operates for grain size below 20 nm which was not clearly achieved in the present investigation. In fact, many features can lead to an activation

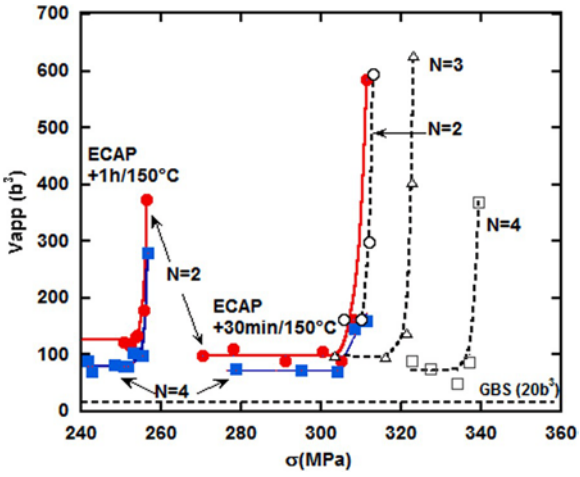

Fig. 9. The apparent activation volume of the alloy processed by ECAE (scaled in b^3) as a function of the applied stress. Open marks: as deformed. Full marks: ECAE and aging at 150 °C.

volume independent of strain and so independent of stress in the representation of Fig. 9: A constant value of V against strain was obtained by Hayes et al. in cryomilled ultrafine-grained aluminum for grain size of 100–170 nm [42]. Beside the low SRS they reported, they showed that the Hall-Petch law was still verified in this range; thus the deformation is controlled by dislocation motion across the grains with a possible competition between dislocation multiplication and dynamic recovery. The same observation has been reported by Semiatin et al. [64] in an Al-Ti-Cu composite. Furthermore, according to Witkin et Lavernia [65] when the grain size decreases to 100 nm or less, grain boundaries act as sources and sinks of dislocations; this supports the results of the molecular dynamics simulations in NC aluminum [66] which indicate that between the conventional intragranular dislocation sources with pileups at large grain sizes and grain-boundary sliding at the finer grain sizes, grain boundary dislocation sources must be considered for the intermediate grain size range.

As indicated above (Section 1), a constant value of V can be obtained when the thermally activated motion of dislocations is related to their interaction with solute atoms [12,67]; in that case, the activation volume can be expressed by [11,68,69]:

$$V = \frac{\sqrt{3}kT}{m_S}(1 - K(Dt_w)^{2/3}) \quad (5)$$

where K is a factor depending on the dislocation motion and solute – dislocation binding energy, D the diffusion coefficient of the precipitating atoms, t_w the waiting time for dislocations to overcome a barrier and $m_S = \partial \mathrm{Ln}\sigma / \partial \mathrm{Ln}\dot{\varepsilon}$. $t_w = \rho_m L b \dot{\varepsilon}$ [70] where ρ_m is the mobile dislocation density and L the effective obstacle spacing or the length of the activated part of the dislocation. On the other hand, it has been demonstrated that when dislocations are locked by solute atoms, t_w depends on the solute concentration as [69]:

$$t_w \propto [(C_1 - C_o)/C_o]^{3/2} \quad (6)$$

where C_1 is the solute concentration on dislocations to be locked and C_o the alloy concentration.

Lloyd [71] has reported in Al-Mg alloys an increase in the SRS accompanied by a decrease in the serrations on the flow curves which were related to a decrease of the role of Mg in pinning dislocations. On the other hand, constant values of m and then V were obtained at a temperature 213 K and strain rate 0.1 min^{-1} [71]; the values extracted from Fig. 18 of the paper correspond to apparent activation volumes of ≈200b^3 and 400b^3 for Mg contents of 4.46% and 2.34% respectively. The increase of V when Mg content decreases was attributed to the role of Mg in defining dislocation interaction type. Thus, as the flow stress results from various contributions, $\sigma = \sigma_D + \sigma_S + \sigma_P + \sigma_{GB}$ (dislocations, solute atoms, precipitates and grain boundaries (Hall-Petch) respectively), $m = \sum_i m_i$ where $m_i = \frac{\Delta\sigma}{\Delta \mathrm{Ln}\dot{\varepsilon}}$ and so $1/V = \sum_i 1/Vi$. σ_P and σ_{GB} are almost athermal and insensitive to strain rate and σ_S is more sensitive than σ_D [71]. Therefore if solute effect exists, it may screen the others so that V≈Vs. For this reason, GB sliding of 10–20b^3 was easily achieved rather in pure metals [11,12]. In the present work, the deformation process is roughly in regime II corresponding to dislocation emission from GB, and the constant values of V are attributed to solute effect mainly Mg. Furthermore, for the grain size investigated, WBDF images of Fig. 10 (N = 3 before compression test) show a clear dislocation activity in the vicinity of a sub-boundary of a grain below 200 nm in size (arrowed in zone 1). Many sources seem to nucleate within the sub-boundary (arrowed in Fig. 10a) whereas many dislocation walls tend to form (double arrows in Fig. 10a). It is worth noting that no pile up is remarked. In region 2 many cells free from dislocations are formed (marked in Fig. 10c). The behavior in the early stages of the compression tests should not differ much so that the constant value of V results in part from GB emission of dislocations in addition to solute atoms contribution. The fact that solute effect is more important at low strain rates i.e. the beginning of the curve V(σ) contradicts the classical predictions since an increase in the SR is equivalent to a decrease in temperature. The mean reason is that at low SR t_w is sufficiently long for a significant segregation of solute atoms to the dislocation core and the effect is more important at high concentrations (Eq. 6).

The decrease in V when N increases can be explained by an increase in the quantity $\rho_m L$ and D through an increase in the total dislocation density on one hand, and to an increase in the amount of Mg atoms pinning dislocations resulting from an eventual dissolution of ultra-fine precipitates formed during quenching on the other hand. This leads to a reduction of the diffusion length of Mg atoms to reach dislocation core; this diffusion was found to be vacancy dependent [72].

Annealing for 30 min at 150 °C enhances diffusion of Mg atoms for N = 2 leading to a further reduction of V. DIC curve recorded at 150 °C (Fig. 11) shows that after 30 min, precipitation sequence reached the β″ step and precipitation is achieved after one hour. In these conditions, the aging peak is not yet reached so that the microstructure should contain GP clusters in addition to a non-equilibrium fraction of precipitates. The precipitate/matrix interface constitutes new FR sources promoting trans-granular slip without need of pile up. Therefore, SRS and then V depend not only on grain size and dislocation density but also on the extent of precipitation [73] From Eq. (6), if C_1 is maintained constant, precipitation decreases C_o and increases t_w; this leads to a reduction of V. In deformed alloys of the present investigation, C_o is leveled since precipitation is completed after 1 h as was deduced from DIC experiments.

As compared to the specimens before aging, the ICS regime is delayed to higher values of σ by precipitation. In fact, the larger domain of σ where V]V* in aged alloys traduces the higher strain rate hardening on the compression curves (Fig. 6). The higher transition stress can be related to a loss in the total length of mobile dislocations due to a pinning by solute atoms and precipitates. We note that for N = 2, V* decreases after aging for 30 min from 160b^3 to 100b^3 than it increases for 60 min (125b^3); this increase can be explained by a decrease of $\rho_m L$ as was shown by Riley and McCormick in Al-Mg-Si alloy [70]. For N = 4 where V* is below 100b^3, the effect of precipitation is negligibly small and V* is kept constant after aging (70–80b^3); this can be explained by an important contribution of GBS. Furthermore, due to the difference in driving forces, it is expected that precipitation takes place before recovery so that

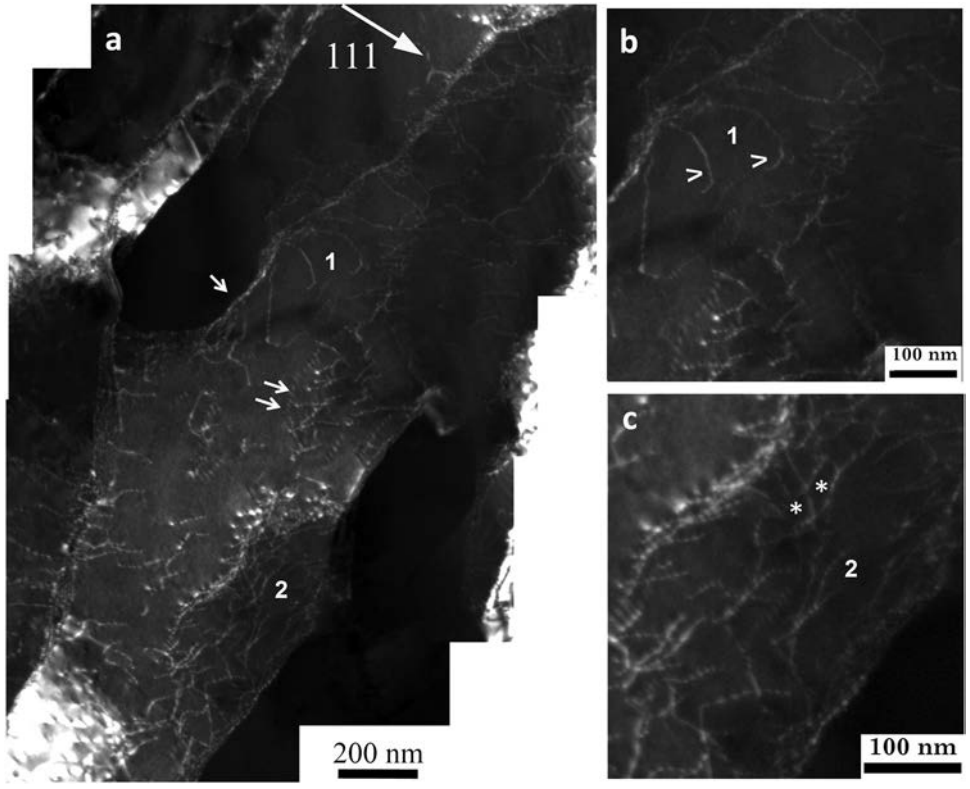

Fig. 10. WBDF image of the alloy for N = 3: in (a) dislocation sources (arrowed) and dislocation tangles (double arrows). (b) Magnification of region 1 showing dislocation activity in grain 100 nm in size. (c) Magnification of region 2 showing sub-grains below 100 nm free from dislocations.

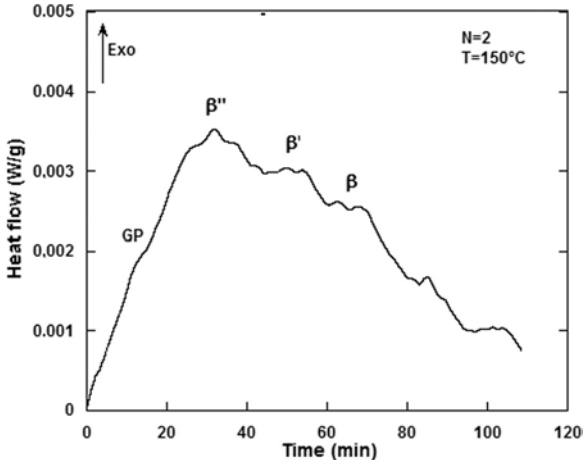

Fig. 11. Differential isothermal thermogram of the alloy for N = 2 recorded at 150 °C. Peak identification was performed referring to [36].

dislocation density should not vary during aging but the total length of mobile dislocations is reduced. Precipitation retains the contribution of GBS for a relatively high stress.

4.2. Positive dependence of V against σ (domain II)

This domain corresponds to high values of stress and high strain rates so that solute effect can be neglected. As was indicated above, there is a high contribution of GB nucleating dislocations in addition to GB sliding. In pure metals, Duhamel et al. [11] have approximated the dependence of V on the applied stress in the low grain size domain by: V]V_{GBS} for $\tau < \tau o^*$and

$$V = V_{GBS} + \left[\frac{2kT/\tau_o^*}{C\delta/b}\right]\left(\frac{\tau^*}{\tau_o^*}\right) \quad 1) \qquad (7)$$

for $\tau > \tau_o^*$. V_{GBS} is the apparent activation volume relative to GBS of the order of $20b^3$, τo^* is the transition stress between GBS and dislocation sliding (DS), $C = t_e/\kappa t_{gb} = v_{gb}/\kappa v_e$ and κ a factor > 1 [11]. The parameter C gives information on the relative importance of the two competitive mechanisms DS and GBS [11,12]: The higher the C, the higher the GB contribution. In the present study C is an adjustable parameter which can be obtained from the representation $V\text{-}V_{GBS}$ vs $(\tau^*\text{-}\tau_c^*)/\tau_o^*$[11]. τ_o^* can be calculated according to the relation $\tau_o^* = \alpha Gb/d_c$ where d_c is the critical grain size. While α, G and b are generally known, τo^* depends on the introduced value of d_c; a referential value of 100 nm is generally adopted for the latter. Using the same values of α, G and b as in Eq. (4) one obtains $\tau_o^* \approx 21.3$ MPa. On the other hand, $\tau^* - \tau_c^*$ was approximated by $\tau - \tau_o$ where τ and τ_o are the experimental data [12] so that the representation becomes $V\text{-}V_{GBS}$ vs $(\tau\text{-}\tau_o)/\tau_o^*$ or vs $(\sigma\text{-}\sigma o)/\sigma_o^*$. At high stress, beyond σ_o, the effect of solute atoms disappears and the ICS regime operates. Nevertheless, as the regime of pure GB sliding and then V_{GBS} is not accessible in the present alloy, V_{GBS} can be safely replaced by the experimental value V* (Fig. 9). The transition stress σ_o can be obtained by extrapolating the ICS straight line to the value $V_{GBS} \approx 20b^3$ (the dashed line on Fig. 9); this leads to σ_o of 313 MPa, 321 MPa and 337 MPa for N = 2, 3 and 4 respectively. These values are almost the same as those corresponding to the actual transition stresses obtained experimentally. From the appropriate representation of Fig. 12, the slope of the ICS straight line in domain II allows calculating the parameter C (Eq. (7)). The obtained values are 9.10^{-4} for N = 2 and N = 3, and 18.10^{-4} for N = 4; they are much smaller than the value 0.2 obtained by Duhamel et al. [11] from SRS experiments in pure copper of grain size≈100 nm, and the value 0.02 obtained by Sun et al. [74] from nanoindentation experiments in pure copper of grain size of 25 nm; the present values show that we are near the

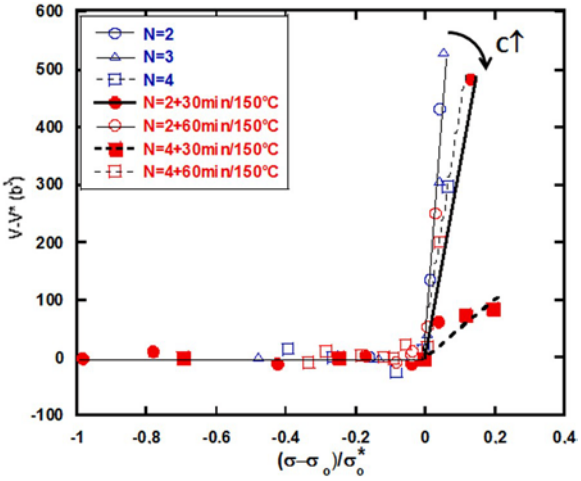

Fig. 12. The representation V-V* vs (σ-σo)/σ of the alloy after ECAE with and without aging at 150 °C (Eq. 7). The slope of the ICS part depends on the GBS contribution.

borderline between of the ICS and CS regimes. Nevertheless, the increase of C for N = 4 indicates an increase in the contribution of GBS.

The effect of aging can also be revealed in the same representation (Fig. 12). In this case, τ * is considered to be the same before and after ageing since in thermal activation analysis, macroscopic changes are considered to affect the athermal component of the stress τa depending on the long range barriers. This allows a direct comparison of the adjustable parameter C. After ageing for 30 min at 150 °C, C value becomes 25.10^{-4} and 160.10^{-4} for N = 2 and N = 4 respectively then it decreases to 9.10^{-4} and 19.10^{-4} after one hour of aging. The increase of C should be related to transition from sub-boundaries to perfect grain boundaries increasing the possibility of GBS.

5. Conclusion

An Al-Mg-Si alloy processed by ECAE up to four passes in a die of characteristic angles ϕ= 90° and ψ = 90°. The alloy was extruded in the as-quenched state. The microstructure was investigated by TEM and ASTAR imaging in the as-deformed and after moderate aging states. From strain rate jump experiments, the stress-dependence of activation volume of deformation was investigated and discussed on the basis of published models.

1) Conventional TEM images revealed grains below 100 nm in size after four passes through the die.
2) Orientation-ASTAR imaging showed elongated grains of various orientations.
3) SRS experiments showed a decrease in the activation volume V up to 70 nm for N = 4. According to published models, grain size achieved and the whole microstructure of the alloy lead to deformation regime consistent with dislocation emission from grain boundaries. This consists with the structure of dislocations in Weak-beam images that revealed a grain-boundary emission.
4) A constant value V* of 70–100b^3 was obtained in the low stress range; it cannot be attributed to pure grain boundary sliding but rather to the effects of solute atoms.
5) At higher stresses, inverse Cottrell-Stokes (ICS) behavior was remarked in which V σ; the results showed that solute effect disappeared and GBS contribution increased with increasing N.
6) Short ageing (30 min at 150 °C) reduces V* ; this was explained by a reduction of the solute atom effect due to precipitation. In the ICS regime, a substantial increase in the contribution of GBS was obtained.

Credit authorship contribution statement

Amel Soula: ECAE processing, mechanical testing, TEM, data curation, **Jean-Philippe Couzinié**: TEM, ASTAR, mechanical testing, manuscript revision, **Hanen Heni**: ECAE processing, mechanical testing, **Julie Bourgon**: TEM, ASTAR, **Yannick Champion**: Mechanical testing, manuscript revision, **Nabil Njah:** Conceptualization and ECAE processing, mechanical testing, data curation, writing, reviewing and editing.

Declaration of Competing Interest

The authors declare that they have no known competing financial interests or personal relationships that could have appeared to influence the work reported in this paper.

Acknowledgements

The authors are grateful to the Direction Générale de la Recherche Scientifique et Technique DGRST (Tunisia) and Centre National de la Recherche Scientifique CNRS (France) for supporting this work under contract 13R/1202.

References

[1] M.R. Langille, B.J. Diak, F. De Geuser, A. Deschamps, G. Guiglionda, Asymmetry of strain rate sensitivity between up- and down-changes in 6000 series aluminum alloys of varying Si content, Mater. Sci. Eng. A 788 (2020) 139517, https://doi.org/10.1016/j.msea.2020.139517
[2] K.S. Havner, On the onset of necking in tensile test, Int. J. Plast. 20 (2004) 965–978, https://doi.org/10.1016/j.ijplas.2003.05.004
[3] A.K. Ghosh, The influence of strain hardening and strain-rate sensitivity on sheet metal forming, J. Eng. Mater. Technol. 99 (1977) 264–274, https://doi.org/10.1115/1.3443530
[4] K.W. Neale, E. Chater, Limit strain predictions for strain-rate sensitive anisotropic sheets, Int. J. Mech. Sci. 22 (1980) 563–574, https://doi.org/10.1016/0020-7403(80)90018-1
[5] A.K. Ghosh, Tensile instability and necking in materials with strain hardening and strain-rate hardening, Acta Metall. 25 (1977) 1413–1424, https://doi.org/10.1016/0001-6160(77)90072-4
[6] E.W. Hart, Theory of the tensile test, Acta Metall. 15 (1967) 351–355, https://doi.org/10.1016/0001-6160(67)90211-8
[7] J.J. Jona, R.A. Holt, C.E. Coleman, Plastic stability in tension and compression, Acta Metall. 24 (1976) 911–918, https://doi.org/10.1016/0001-6160(76)90039-0
[8] S. Nemat-Nasser, Y.L. Li, Flow stress of fcc polycrystals with application to OFHC Cu, Acta Mater. 46 (1998) 565–577, https://doi.org/10.1016/S1359-6454(97)00230-9
[9] L. Lu, R. Schwaiger, Z.W. Shan, M. Dao, K. Lu, S. Suresh, Nano-sized twins induce high rate sensitivity of flow stress in pure copper, Acta Mater. 53 (2005) 2169–2179, https://doi.org/10.1016/j.actamat.2005.01.031
[10] J.P. Couzinie, L. Lilensten, Y. Champion, G. Dirras, L. Perriere, I. Guillot, On the room temperature deformation mechanisms of a TiZrHfNbTa refractory high-entropy alloy, Mater. Sci. Eng. A 645 (2015) 255–263, https://doi.org/10.1016/j.msea.2015.08.024
[11] C. Duhamel, Y. Bréchet, Y. Champion, Activation volume and deviation from Cottrell–Stokes law at small grain size, Int. J. Plast. 26 (2010) 747–757, https://doi.org/10.1016/j.ijplas.2009.10.003
[12] Y. Champion, Competing regimes of rate dependent plastic flow in ultrafine grained metals, Mater. Sci. Eng. A 560 (2013) 315–320, https://doi.org/10.1016/j.msea.2012.09.072
[13] A. van den Beukel, Theory of the effect of dynamic strain aging on mechanical properties, Phys. Stat. Sol. (a) 30 (1975) 197–206, https://doi.org/10.1002/pssa.2210300120
[14] Z.S. Basinski, Forest hardening in face centered cubic metals, Scr. Met. 8 (1974) 1301–1308, https://doi.org/10.1016/0036-9748(74)90350-0
[15] H. Conrad, J. Narayan, Mechanisms for grain size hardening and softening in Zn, Acta Mater. 50 (2002) 5067–5078, https://doi.org/10.1016/S1359-6454(02)00357-9
[16] H. Conrad, J. Narayan, On the grain size softening in nanocrystalline materials, Scr. Mater. 42 (2000) 1025–1030, https://doi.org/10.1016/S1359-6462(00)00320-1
[17] Y.M. Wang, A.V. Hamza, E. Ma, Temperature-dependent strain rate sensitivity and activation volume of nanocrystalline Ni, Acta Mater. 54 (2006) 2715–2726, https://doi.org/10.1016/j.actamat.2006.02.013
[18] V.M. Segal, V.I. Reznikov, A.E. Dorbyshevskity, V.I. Kopylov, Plastic working of metals by simple shear, Russ. Metall. 1 (1981) 99.
[19] V. Segal, Modes and processes of severe plastic deformation (SPD), Materials 11 (2018) 1175, https://doi.org/10.3390/ma1107117

[20] C. Lee, H.K. Seok, J.Y. Suh, Microstructural evolutions of the Al strip prepared by cold rolling and continuous equal channel angular pressing, Acta Mater. 50 (2002) 4005–4019, https://doi.org/10.1016/S1359-6454(02)00200-8
[21] L.R.C. Malheiros, R.B. Figueiredo, T.G. Langdon, Grain size and microhardness evolution during annealing of a magnesium alloy processed by high-pressure torsion, J. Mater. Res. Technol. 4 (2015) 14–17, https://doi.org/10.1016/j.jmrt.2014.10.008
[22] X. Chen, C. Liu, Y. Wan, S. Jiang, Z. Chen, Y. Zhao, Grain refi mechanisms in gradient nanostructured AZ31B Mg alloy prepared via rotary swaging, Metall. Mater. Trans. A 52 (2021) 4053–4065, https://doi.org/10.1007/s11661-021-06364-9
[23] Y. Yang, X. Chen, J. Nie, K. Wei, Q. Mao, F. Lu, Y. Zhao, Achieving ultra-strong Magnesium–lithium alloys by low-strain rotary swaging, Mater. Res. Lett. 9 (2021) 255–262, https://doi.org/10.1080/21663831.2021.1891150
[24] Y. Wan, B. Tang, Y. Gao, L. Tang, G. Sha, B. Zhang, N. Liang, C. Liu, S. Jiang, Z. Chen, X. Guoa, Y. Zhao, Bulk nanocrystalline high-strength magnesium alloys prepared via rotary swaging, Acta Mater. 200 (2020) 274–286, https://doi.org/10.1016/j.actamat.2020.09.024
[25] S. Van Petegem, J. Zimmermann, H. Van Swygenhove, Yield point phenomenon during strain rate change in nanocrystalline Ni–Fe, Scr. Mater. 65 (2011) 217–220, https://doi.org/10.1016/j.scriptamat.2011.04.007
[26] A.J. Detor, C.A. Schuh, Tailoring and patterning the grain size of nanocrystalline alloys, Acta Mater. 55 (2007) 371–379, https://doi.org/10.1016/j.actamat.2006.08.032
[27] Y. Zhou, U. Erb, K.T. Aust, The role of interface volume fractions in the nanocrystalline to amorphous transition in fully dense materials, Philos. Mag. 87 (2007) 5749–5761, https://doi.org/10.1080/14786430701716987
[28] R.Z. Valiev, R.K. Islamgliev, I.V. Alexandrov, Bulk nanostructured materials from severe plastic deformation, Prog. Mater. Sci. 45 (2000) 103–189, https://doi.org/10.1016/S0079-6425(99)00007-9
[29] X.H. An, S.D. Wu, Z.F. Zhang, Evolution of microstructural homogeneity in copper processed by high-pressure torsion, Scr. Mater. 63 (2010) 560–563, https://doi.org/10.1016/j.scriptamat.2010.05.030
[30] Z.C. Duan, N.Q. Chinh, C. Xu, T.G. Langdon, Developing processing routes for the equal-channel angular pressing of age-hardenable aluminum alloys, Metall. Mater. Trans. A 41 (2010) 802–809, https://doi.org/10.1007/s11661-009-0020-1
[31] K.R. Cardoso, D.N. Travessa, W.J. Botta, A.M. Jorge Jr., High strength AA7050 Al alloy processed by ECAP: microstructure and mechanical properties, Mater. Sci. Eng. A. 528 (2011) 5804–5811, https://doi.org/10.1016/j.msea.2011.04.007
[32] V.M. Segal, Engineering and commercialization of equal channel angular extrusion (ECAE), Mater. Sci. Eng. A 386 (2004) 269–276, https://doi.org/10.1016/j.msea.2004.07.023
[33] C.M. Cepeda-Jim_enez, J.M. García-Infanta, O.A. Ruano, F. Carre~no, Mechanical properties at room temperature of an Al-Zn-Mg-Cu alloy processed by equal channel angular pressing, J. Alloy. Compd. 509 (2011) 8649–8656, https://doi.org/10.1016/j.jallcom.2011.06.070
[34] C.M. Cepeda-Jim_enez, J.M. García-Infanta, E.F. Rauch, J.J. Blandin, O.A. Ruano, F. Carreno, Influence of processing severity during equal-channel angular pressing on the microstructure of an Al-Zn-Mg-Cu alloy, Metall. Mater. Trans. A 43 (2012) 4224–4236, https://doi.org/10.1007/s11661-012-1206-5
[35] J. Hirsch, Recent development in aluminum for automotive applications, Trans. Nonferrous Met. Soc. China 24 (7) (. 2014) 1995–2002, https://doi.org/10.1016/S1003-6326(14)63305-7
[36] M. Liu, T. Jiang, J. Wang, Q. Liu, Z. Wu, Y. Yu, P.C. Skaret, H.J. Roven, Aging behavior and mechanical properties of 6013 aluminum alloy processed by severe plastic deformation, Trans. Nonferrous Met. Soc. China 24 (2014) 3858–3865, https://doi.org/10.1016/S1003-6326(14)63543-3
[37] X.H. An, S.D. Wu, Z.F. Zhang, R.B. Figueiredo, N. Gao, T.G. Langdon, Evolution of microstructural homogeneity in copper processed by high-pressure torsion, Scr. Mater. 63 (2010) 560–563, https://doi.org/10.1016/j.scriptamat.2010.05.030
[38] R.Z. Valiev, A.V. Korznikov, I.V. Alexandrov, Nanomaterials produced by severe plastic deformation: an introduction, Ann. Chim. -Sci. Mat. 27 (2002) 1–2.
[39] J. Chen, C. Liu, Microstructure evolution of precipitates in AlMgSi(Cu) alloys, Chin. J. Nonferrous Met. 21 (2011) 2352–2360 (in Chinese).
[40] H. Liu, G. Zhao, C. Liu, L. Zuo, Effects of different tempers on precipitation hardening of 6000 series aluminium alloys, Trans. Nonferrous Met. Soc. China 17 (2007) 122–127, https://doi.org/10.1016/S1003-6326(07)60059-4
[41] M. Murayama, Z. Horita, K. Hono, Microstructure of two-phase Al-1.7 at% Cu alloy deformed by equal-channel angular pressing, Acta Mater. 49 (2001) 21–29, https://doi.org/10.1016/S1359-6454(00)00308-6
[42] R.W. Hayes, D. Witkin, F. Zhou, E.J. Lavernia, Deformation and activation volumes of cryomilled ultrafine-grained aluminum, Acta Mater. 52 (2004) 4259–4271, https://doi.org/10.1016/j.actamat.2004.05.042
[43] Y. Iwahashi, J. Wang, M. Horita, M. Nemoto, T.G. Langdon, Principle of equal channel angular pressing for the processing of ultra-fine grained materials, Scr. Mater. 35 (1996) 143–146, https://doi.org/10.1016/1359-6462(96)00107-8
[44] E.F. Rauch, J. Portillo, S. Nicolopoulos, D. Bultreys, S. Rouvimov, P. Moeck, Automated nanocrystal orientation and phase mapping in the transmission electron microscope on the basis of precession electron diffraction, Zeit ., Krist. 225 (2–3) (2010) 103–109, https://doi.org/10.1524/zkri.2010.1205
[45] B.J. Diak, K.R. Upadhyaya, S. Saimoto, Characterization of thermodynamic response by materials testing, Prog. Mater. Sci. 43 (1998) 223–363, https://doi.org/10.1016/S0079-6425(98)00007-3
[46] Z. Zribi, H.H. Ktari, F. Herbst, V. Optasanu, N. Njah, EBSD, XRD and SRS characterization of a casting Al-7wt%Si alloy processed by equal channel angular extrusion: Dislocation density evaluation, Mater. Charact. 153 (2019) 190–198, https://doi.org/10.1016/j.matchar.2019.04.044
[47] A.K. Gupta, K.J. Lloyd, S.A. Court, Precipitation hardening processes in Al-0.4% Mg-1.3%Si-0.25%Fe aluminum alloy [J], Mater. Sci. Eng. A 301 (2001) 140–146, https://doi.org/10.1016/S0921-5093(00)01814-1
[48] W.F. Miao, D.E. Laughlin, Precipitation hardening in aluminum alloy 6022, Scr. Mater. 40 (1999) 873–878, https://doi.org/10.1016/S1359-6462(99)00046-9
[49] U.F. Kocks, H. Mecking, Physics and phenomenology of strain hardening: the FCC case, Prog. Mater. Sci. 48 (2003) 171–273, https://doi.org/10.1016/S0079-6425(02)00003-8
[50] O. Bouaziz, S. Allain, C. Scott, Effect of grain and twin boundaries on the hardening mechanisms of twinning-induced plasticity steels, Scr. Mater. 58 (2008) 484–487, https://doi.org/10.1016/j.scriptamat.2007.10.050
[51] Q. Wei, Strain rate effects in the ultrafine grain and nanocrystalline regimes-influence on some constitutive responses, J. Mater. Sci. 42 (2007) 1709–1727, https://doi.org/10.1007/s10853-006-0700-9
[52] A. Rebhi, T. Makhlouf, N. Njah, Y. Champion, J.P. Couzinié, Characterization of aluminum processed by equal channel angular extrusion: Effect of processing route, Mater. Charact. 60 (2009) 1489–1495, https://doi.org/10.1016/j.matchar.2009.08.004
[53] H.J. Roven, M. Liu, J.C. Werenskiold, Dynamic precipitation during severe plastic deformation of an Al–Mg–Si aluminium alloy, Mater. Sci. Eng. A 483–484 (2008) 54–58, https://doi.org/10.1016/j.msea.2006.09.142
[54] S. Van Petegem, J. Zimmermann, H. Van Swygenhoven, Yield point phenomenon during strain rate change in nanocrystalline Ni–Fe, Scr. Mater. 65 (2011) 217–220, https://doi.org/10.1016/j.scriptamat.2011.04.007
[55] H.G. Champion, M.S. Duesbery, S. Saimoto, Elimination of machine transient effects during plastic strain rate changes, Scr. Met. 17 (1983) 135–140, https://doi.org/10.1016/0036-9748(83)90086-8
[56] M. Carlone, S. Saimoto, Precision Strain Rate Sensitivity Measurement Using the Step-ramp Method, Exp. Mech. 36 (1996) 360–366, https://doi.org/10.1007/BF02328579
[57] P.G. McCormick, The effect of strain on the ageing time for serrated yielding in an AI-Mg-Si alloy, Acta Met. 22 (1974) 489–493, https://doi.org/10.1016/0001-6160(74)90102-3
[58] Y. Wang, S. Goel, J.L. Sun, Y.M. Zhu, H. Yuan, J.T. Wang, The effect of temperature on activation volume of ultrafine grained tantalum, or 2018, Int. J. Refract. Met. Hard Mater. (2017), https://doi.org/10.1016/j.ijrmhm.2017.11.029
[59] C.Y. Yu, P.W. Kao, C.P. Chang, Transition of tensile deformation behaviors in ultrafine-grained aluminum, Acta Mater. 53 (2005) 4019–4028, https://doi.org/10.1016/j.actamat.2005.05.005
[60] A.M. Hodge, Y.M. Wang, T.W. Barbee, Mechanical deformation of high-purity sputter-deposited nano-twinned copper, Scr. Mater. 59 (2008) 163–166, https://doi.org/10.1016/j.scriptamat.2008.02.048
[61] T. Sakai, A. Belyakov, R. Kaibyshev, H. Miura, J.J. Jonas, Dynamic and post-dynamic recrystallization under hot, cold and severe plastic deformation conditions, Prog. Mater. Sci. 60 (2014) 130–207, https://doi.org/10.1016/j.pmatsci.2013.09.002
[62] H. Van Swygenhoven, A. Caro, Plastic behavior of nanophase metals studied by molecular dynamics, Phys. Rev. B 58 (1998) 11246–11251, https://doi.org/10.1103/PhysRevB.58.11246
[63] H. Van Swygenhoven, M. Spaczer, A. Caro, D. Farkas, Competing plastic deformation mechanisms in nanophase metals, Phys. Rev. B 60 (1999) 22–25, https://doi.org/10.1103/PhysRevB.60.22
[64] S.L. Semiatin, K.V. Jata, M.D. Uchic, P.B. Berbon, D.E. Matejczyk, C.C. Bampton, Plastic flow and fracture behavior of an Al-Ti-Cu nanocomposite, Scr. Mater. 44 (2001) 395–400, https://doi.org/10.1016/S1359-6462(00)00612-6
[65] D.B. Witkin, E.J. Lavernia, Synthesis and mechanical behavior of nanostructured materials via cryomilling, Prog. Mater. Sci. 51 (2006) 1–60, https://doi.org/10.1016/j.pmatsci.2005.04.004
[66] V. Yamakov, D. Wolf, M. Salazar, S.R. Phillpot, H. Gleiter, Length-scale effects in the nucleation of extended dislocations in nanocrystalline Al by molecular-dynamics simulation, Acta Mater. 49 (2001) 2713–2722, https://doi.org/10.1016/S1359-6454(01)00167-7
[67] S.H. van den Brink, A. van den Beukel, P.G. McCormick, Strain rate sensitivity and the portevin-le chatelier effect in Au–Cu alloys, Phys. Stat. Sol. (a) 30 (1975) 469–477, https://doi.org/10.1002/pssa.2210300205
[68] H.J. Harun, P.G. McCormick, Effect of precipitation hardening on strain rate sensitivity and yield behaviour in an Al-Mg-Si alloy, Acta Met. 27 (1979) 155–159, https://doi.org/10.1016/0001-6160(79)90067-1
[69] M.A. Afifi, Y.C. Wang, X. Cheng, S. Li, T.G. Langdon, Strain rate dependence of compressive behavior in an Al-Zn-Mg alloy processed by ECAP, J. Alloy. Compd. 791 (2019) 1079–1087, https://doi.org/10.1016/j.jallcom.2019.03.390
[70] D.M. Riley, P.G. McCormick, The effect of precipitation hardening on the Portevin-Le Chatelier effect in an Al-Mg-Si alloy, Acta Met. 25 (1977) 181–185, https://doi.org/10.1016/0001-6160(77)90121-3
[71] D.J. Lloyd, The deformation of commercial aluminum-magnesium alloys (https://doi:), Metal. Trans. A 11 (1980) 1287–1294, https://doi.org/10.1007/bf02653482
[72] R.K.W. Marceau, G. Sha, R.N. Lumley, S.P. Ringer, Evolution of solute clustering in Al–Cu–Mg alloys during secondary ageing, Acta Mater. 58 (2010) 1795–1805, https://doi.org/10.1016/j.actamat.2009.11.021
[73] Y.H. Zhao, X.Z. Liao, S. Cheng, E. Ma, Y.T. Zhu, Simultaneously increasing the ductility and strength of nanostructured alloys, Adv. Mater. 18 (2006) 2280–2283, https://doi.org/10.1002/adma.200600310
[74] W. Sun, Y. Jiang, G. Sun, J. Hu, T. Zhou, Z. Jiang, J. Lian, Nanoindentation creep behavior and its relation to activation volume and strain rate sensitivity of nanocrystalline Cu, Mater. Sci. Eng. A 751 (2019) 35–41, https://doi.org/10.1016/j.msea.2019.02.027